UNIVERSITY OF LEEDS

This is a repository copy of *On the influence of a translating inner core in models of outer core convection*.

White Rose Research Online URL for this paper:
http://eprints.whiterose.ac.uk/80886/

Version: Accepted Version

Article:

Davies, CJ, Silva, L and Mound, J (2013) On the influence of a translating inner core in models of outer core convection. Physics of the Earth and Planetary Interiors, 214. 104 - 114. ISSN 0031-9201

https://doi.org/10.1016/j.pepi.2012.10.001

Reuse
Unless indicated otherwise, fulltext items are protected by copyright with all rights reserved. The copyright exception in section 29 of the Copyright, Designs and Patents Act 1988 allows the making of a single copy solely for the purpose of non-commercial research or private study within the limits of fair dealing. The publisher or other rights-holder may allow further reproduction and re-use of this version - refer to the White Rose Research Online record for this item. Where records identify the publisher as the copyright holder, users can verify any specific terms of use on the publisher's website.

Takedown
If you consider content in White Rose Research Online to be in breach of UK law, please notify us by emailing eprints@whiterose.ac.uk including the URL of the record and the reason for the withdrawal request.

White Rose
university consortium
Universities of Leeds, Sheffield & York

eprints@whiterose.ac.uk
https://eprints.whiterose.ac.uk/

On the influence of a translating inner core in models of outer core convection

C. J. Davies[a,*], L. Silva[a], J. Mound[a]

[a]*School of Earth and Environment, University of Leeds, Leeds LS2 9JT, UK*

Abstract

It has recently been proposed that the hemispheric seismic structure of the inner core can be explained by a self-sustained rigid-body translation of the inner core material, resulting in melting of the solid at the leading face and a compensating crystallisation at the trailing face. This process induces a hemispherical variation in the release of light elements and latent heat at the inner-core boundary, the two main sources of thermochemical buoyancy thought to drive convection in the outer core. However, the effect of a translating inner core on outer core convection is presently unknown. In this paper we model convection in the outer core using a nonmagnetic Boussinesq fluid in a rotating spherical shell driven by purely thermal buoyancy, incorporating the effect of a translating inner core by a time-independent spherical harmonic degree and order 1 (Y_1^1) pattern of heat-flux imposed at the inner boundary. The analysis considers Rayleigh numbers up to 10 times the critical value for onset of nonmagnetic convection, a parameter regime where the effects of the inhomogeneous boundary condition are expected to be most pronounced, and focuses on varying q^*, the amplitude of the imposed boundary anomalies. The presence of inner boundary anomalies significantly affects the behaviour of the model system. Increasing q^* leads to flow patterns dominated by azimuthal jets that span large regions of the shell where radial motion is significantly inhibited. Vigorous convection becomes increasingly confined to isolated regions as q^* increases; these regions do not drift and always occur in the hemisphere subjected to a higher than average boundary heat-flux. Effects of the inner boundary anomalies are visible at the outer boundary in all models considered. At low q^* the expression of inner boundary effects at the core surface is a difference in the flow amplitude between the two hemispheres. As q^* increases the spiralling azimuthal jets driven from the inner boundary are clearly visible at the outer boundary. Finally, our results suggest that, when the system is heated from below, a Y_1^1 heat-flux pattern imposed on the inner boundary has a greater overall influence on the spatio-temporal behaviour of the flow than the same pattern imposed at the outer boundary.

Keywords: Inner core translation, outer core convection, zonal flows, inhomogeneous heat-flux

*Corresponding author

Email address: `c.davies@earth.leeds.ac.uk; tel: +44 (0) 113 3435543` (C. J. Davies)

1. Introduction

Free thermal convection of the inner core, driven by either radiogenic heating (Jeanloz and Wenk, 1988) or secular cooling (Buffett, 2009), has been proposed to explain the observed cylindrical anisotropy in inner core P-wave velocity (Morelli et al., 1986; Woodhouse et al., 1986). For this proposition to be viable the inner core must be (at least partially) unstably stratified. Such a stratification may arise if the inner core temperature gradient exceeds the adiabatic gradient at the relevant pressure-temperature conditions; previous models suggest this may be true at present and was more likely in the past (Buffett, 2009; Deguen and Cardin, 2009, 2011). Recent work suggests that the thermal conductivity of the outer core is significantly higher than previously thought (Pozzo et al., 2012; de Koker et al., 2012), which may affect the viability of thermal inner core convection, although these calculations pertain to the liquid phase only. Another possibility is that the inner core is compositionally unstable, which may arise if the amount of light element that remains in the solid on freezing decreases with time (Deguen and Cardin, 2011; Alboussière and Deguen, 2012). In reality the net inner core density gradient is determined by a combination of thermal and chemical effects. Uncertainties in key parameters such the cooling rate at the inner core boundary (ICB), the core-mantle boundary (CMB) heat-flux, and the partition coefficients of the various light elements in the core prevent an unequivocal determination of the inner core stratification and so inner core convection remains a realistic possibility. If the inner core does convect the preferred model likely depends on the bulk viscosity (Deguen and Cardin, 2011). If the viscosity is sufficiently large the inner core could undergo a translational mode of convection involving an eastward drift of inner core material (Monnereau et al., 2010; Alboussière et al., 2010). This mode has been used to explain an observed asymmetry in seismic velocities between eastern and western hemispheres (Tanaka and Hamaguchi, 1997; Niu and Wen, 2001; Waszek et al., 2011) and the existence of a seismically slow layer in the bottom ~ 150 km of the outer core (Souriau and Poupinet, 1991; Kennett et al., 1995; Zou et al., 2008).

Convection in the outer core is driven by a combination of thermal and chemical buoyancy forces that in turn result from the Earth's slow cooling (e.g. Buffett et al., 1996; Gubbins et al., 2003, 2004). These buoyancy forces are likely to be strongest near the base of the outer core (Davies and Gubbins, 2011) where inner core growth due to freezing of the liquid iron alloy releases latent heat (Verhoogen, 1961), and a light component of the outer core mixture, probably oxygen (Alfè et al., 1999), remains in the liquid to provide a source of compositional buoyancy (Braginsky, 1963). Models of outer core convection usually assume that light element and latent heat release at the ICB are spherically symmetric and that convection is driven uniformly from below (e.g. Braginsky and Roberts, 1995; Anufriev et al., 2005); however, the translational mode of inner core convection requires freezing in the western hemisphere and melting in the eastern hemisphere (Monnereau et al., 2010; Alboussière et al., 2010). The asymmetry arises because the eastward drift of inner core material induces a west to east density gradient with heavy material on the freezing western side; hydrostatic adjustment shifts the centre of mass of the inner core eastward so that the eastern part of the inner core is above the melting temperature, leading to localised melting

(Alboussière et al., 2010). Outer core convection is then driven non-uniformly from below: in the western hemisphere, release of latent heat and light elements create outward buoyancy fluxes that drive convection; in the eastern hemisphere, latent heat is absorbed and no light elements are released, thereby creating a negative buoyancy flux.

In this paper we investigate the possible influence of a translating inner core on outer core convection using a simple model of a rotating fluid-filled spherical shell. To incorporate hemispherical variations induced by a translating inner core we note that the turnover time of outer core convection, $\tau_{\mathrm{c}} = d/U \sim 10^2$ yrs (Gubbins, 2007), is much shorter than both the turnover time of the translational mode, $\tau_{\mathrm{ic}} = l/v_t \sim 10^8$ yrs, and the timescale for inner core growth $\tau_{\mathrm{g}} = l/v_g \sim 10^9$ yrs (Labrosse et al., 2001). Here d is the outer core shell thickness, U a characteristic outer core velocity, l the inner core radius, $v_t \sim 10^{-10}$ m s^{-1} (Alboussière et al., 2010) a characteristic translational velocity and $v_g \sim 10^{-11}$ m s^{-1} a characteristic inner core growth rate. We therefore assume that, on the timescales associated with outer core convection, both the ICB and the thermochemical anomalies resulting from translation are stationary and can be modelled as a time-independent bottom boundary condition in the outer core convection simulation. We further assume that this boundary condition takes the form of a fixed flux. The outer core is well-mixed on timescales associated with inner core convection, implying that the latter should be modelled with an isothermal and chemically homogeneous ICB. Outer core convection must then respond to lateral variations in thermal and chemical fluxes at the ICB induced by the translating inner core. The bottom boundary condition is specified by the pattern and amplitude of thermochemical flux.

In this paper we approximate the pattern of hemispherical melting and freezing by a Y_1^1 spherical harmonic. The amplitude of the anomaly is measured by q^*, the ratio of the peak-to-peak variation and the average flux through the boundary (see §2 for the mathematical definition). Estimates of q^* for the Earth are highly uncertain. The thermal contribution depends on physical properties of the inner and outer cores, some of which are known to within a factor of 3 at the relevant pressure-temperature conditions (Stacey, 2007), and gross quantities such as the CMB heat-flux, which can only be estimated to within a factor of 3–4 at present (Lay et al., 2009) and vary significantly over time (e.g. Nimmo et al., 2004; Nimmo, 2007). The chemical contribution depends on the relative abundance of light elements in both cores (i.e on the part of the ICB density jump not due to the phase change) and on mixing properties of the core alloy, which are likely to be non-ideal (Helffrich, 2012) and exhibit complex dependencies on partition coefficients (Alboussière et al., 2010; Deguen and Cardin, 2011).

A simple estimate of q^*, q_e^*, can be obtained by neglecting chemical effects and assuming that the only thermal buoyancy source at the ICB is latent heat (thus neglecting secular cooling and the effect of the adiabat, both of which are likely to be smaller than the latent heat (Davies and Gubbins, 2011)). The average ICB heat-flux per unit area, q_{L}, is then (Gubbins et al., 2003)

$$q_{\mathrm{L}} = \rho_{\mathrm{i}} L \frac{\mathrm{d}r_{\mathrm{i}}}{\mathrm{d}t} = \rho_{\mathrm{i}} L v_g, \tag{1}$$

where r_{i} is the ICB radius, ρ_{i} the inner core density, and L the latent heat. An expression for the maximum heat-flux is obtained by replacing v_g with the translation velocity, v_t, in

(1). Assuming that the absolute value of the maximum and minimum heat-flux anomaly are equal gives the estimate

$$q_e^* = \frac{2v_t}{v_g}. \tag{2}$$

Using values from Alboussière et al. (2010) gives present-day estimates in the range $1 \lesssim q_e^* \lesssim 30$ for a CMB heat-flux ranging from 8–11 TW. We vary q^* in our simulations to exhibit the dependence of the convection on this parameter.

This paper is organised as follows. In §2 we describe the numerical model used to simulate convection in the outer core. In §3.1 we present models with a laterally-varying Y_1^1 inner boundary condition and a spherically symmetric outer boundary condition. We discuss the changes in spatio-temporal behaviour that emerge as q^* is varied and conduct a detailed analysis of the mechanisms that drive large-scale flows in our models. In §3.2 we briefly discuss models with a laterally-varying Y_1^1 outer boundary condition and a spherically symmetric inner boundary condition and compare to the results obtained in §3.1. Discussion and conclusions are presented in §4.

2. Methods

We consider a model of convection in a rotating spherical shell that incorporates lateral variations in the thermodynamic boundary conditions. A Boussinesq fluid of constant thermal diffusivity, κ, constant coefficient of thermal expansion, α, and constant viscosity, ν, is confined to a rotating spherical shell of thickness $d = r_\mathrm{o} - r_\mathrm{i}$. Here r_i and r_o are respectively the inner and outer boundary radii in spherical polar coordinates, (r, θ, ϕ). The fluid rotates about the axial $\mathbf{z}$-axis with angular velocity Ω. To relate our results to previous studies and to avoid double diffusive effects, which we regard as an unnecessary complication at this stage, we consider a chemically homogeneous system heated from below, the analogue of outer core convection driven by latent heat release at the inner boundary with no compositional buoyancy. With no flow, the basic steady state temperature, T_0, is maintained such that $\nabla T_0 = -(\beta/r^2)\hat{\mathbf{r}}$, where β measures the amplitude of the basic state radial temperature gradient, $\mathbf{r}$ is the radial position vector and a hat denotes a unit vector. The total temperature field $T = T_0 + T'$, where T' is the deviation from the basic state temperature. Scaling length by the shell thickness, d, time by the thermal diffusion time, d^2/κ, and temperature by β/d, the nondimensional perturbation equations are

$$\frac{E}{Pr}\left(\frac{\partial \mathbf{u}}{\partial t} + (\mathbf{u}\cdot\nabla)\mathbf{u}\right) + \mathbf{z}\times\mathbf{u} = -\nabla\bar{P} + RaT'\mathbf{r} + E\nabla^2\mathbf{u}, \tag{3}$$

$$\frac{\partial T'}{\partial t} + (\mathbf{u}\cdot\nabla)T' = \nabla^2 T' + \mathbf{u}\cdot(\beta r^{-2})\hat{\mathbf{r}}, \tag{4}$$

$$\nabla\cdot\mathbf{u} = 0. \tag{5}$$

The pressure gradient $\nabla\bar{P}$, is removed from the problem by taking the curl of (3). The Ekman number E, Prandtl number Pr, and modified Rayleigh number Ra are

$$E = \frac{\nu}{2\Omega d^2}, \quad Pr = \frac{\nu}{\kappa}, \quad Ra = \frac{\alpha g \beta}{2\Omega\kappa}, \tag{6}$$

where g is the gravitational acceleration at the outer boundary. Gravity varies linearly with radius. The radius ratio, $r_\mathrm{i}/r_\mathrm{o}$, of the shell is set to 0.35.

The fluid velocity $\mathbf{u}$ is decomposed into toroidal and poloidal components,

$$\mathbf{u} = \nabla \times \mathcal{T}\mathbf{r} + \nabla \times \nabla \times \mathcal{P}\mathbf{r}. \tag{7}$$

The toroidal, $\mathcal{T}$, and poloidal, $\mathcal{P}$, scalars along with the temperature T' are expanded in spherical harmonics $Y_l^m(\theta, \phi)$. The radial dependence of all variables is computed using finite differences.

We use no-slip and impenetrable inner and outer boundaries, requiring

$$\mathbf{u}(r_\mathrm{i}) = \mathbf{u}(r_\mathrm{o}) = 0. \tag{8}$$

We also fix the heat-flux on both boundaries. Lateral variations in heat-flux on the inner boundary (IB) and outer boundary (OB) are modelled using the method described in (Gibbons et al., 2007). In all models the pattern of the boundary variation is a Y_1^1 spherical harmonic. The amplitude of the anomalies is measured by the parameter q^*, defined as the ratio of the peak-to-peak variation in boundary heat-flux and the average boundary heat-flux

$$q^* = \frac{q_{max} - q_{min}}{q_0} = \frac{2q_{max}}{q_0}, \tag{9}$$

where q_{max} and q_{min} are the maximum and minimal values of the boundary anomaly. q_0 is a nondimensional measure of the average boundary heat-flux per unit area, $q_0 = (1/r^2)$, and is approximately a factor of 8 larger at the IB than at the OB. Hence, to impose the same value of q_{max} at the IB and OB requires that the value of q^* is 8 times larger in the variable OB heat-flux calculation compared to the variable IB heat-flux calculation.

The governing equations (3)–(5) are solved using a pseudo-spectral method. Detailed descriptions of the code are given in Willis et al. (2007) and Davies et al. (2011).

3. Results

Table 1 lists all simulations conducted for this work. In order to facilitate comparisons and to elucidate the effect of the laterally-varying IB condition, we fix the values of E and Pr and vary Ra and q^*. For simplicity we use the value $Pr = 1$ throughout. The Ekman number is the major computational challenge. The lowest value of E used in a numerical simulation is $\sim 5{\times}10^{-7}$ (Kageyama et al., 2008); very few models have been conducted in this parameter regime, which is still many orders of magnitude higher than the value $E \sim 10^{-15}$ appropriate to Earth's outer core. We fix $E = 10^{-5}$, which is low enough for rotation to dominate in our calculations but high enough to conduct a suite of simulations run for long enough to obtain time-averages that span many time units. At this value of E a linear stability analysis (see Gibbons et al. (2007) and Davies et al. (2009) for details) with our chosen boundary conditions and value of Pr shows that the most unstable azimuthal wavenumber, $m_c = 9$, and the corresponding value of the critical Rayleigh number, $Ra_c = 25.5$, for the onset of non-magnetic convection with homogeneous boundaries ($q^* = 0$). We focus on the parameter range $3Ra_c \leq Ra \leq 10Ra_c$, where we expect the influence of the inhomogeneous boundary condition to be most pronounced. If boundary effects are not important in this regime we would anticipate that they be less significant in the core where Ra is likely to be many times supercritical (Gubbins, 2001; Davies and Gubbins, 2011).

All simulations were started from the same initial condition with $\mathbf{u} = 0$ and arbitrary three dimensional seed perturbations superimposed on the basic state temperature profile. The spatial resolution required to achieve a given level of spectral convergence increases with Ra. At the lowest values of Ra we found that $N_{max} = 90$ radial points and maximum harmonic degree $L_{max} = 84$ produced a drop of four orders of magnitude between wavenumbers with highest and lowest energy. At the highest values of Ra, $N_{max} = 120$ and $L_{max} = 128$ were required to obtain the same convergence.

For the subsequent discussion we define the dimensionless kinetic energy $K = K_{\mathcal{T}} + K_{\mathcal{P}}$, where the toroidal and poloidal components are given respectively by

$$\begin{aligned} K_{\mathcal{T}} &= \frac{1}{2}\left\langle |\nabla \times \mathcal{T}\mathbf{r}|^2 \right\rangle, \\ K_{\mathcal{P}} &= \frac{1}{2}\left\langle |\nabla \times \nabla \times \mathcal{P}\mathbf{r}|^2 \right\rangle, \end{aligned}$$

and angled brackets indicate a time average over the length of the run quoted in Table 1. The zonal part of the toroidal energy, $K_{\mathcal{T}}^{z}$, is obtained by retaining only the $m = 0$ harmonic coefficient.

Our choice of nondimensionalisation means that the Péclet number, $Pe = Ud/\kappa = \sqrt{2K/V_s}$, where V_s is the volume of the spherical shell, measures the amplitude of the velocity U. With all other parameters fixed, increasing Ra leads to an increase in Pe while the ratios $K_{\mathcal{T}}/K$ and $K_{\mathcal{T}}^{z}/K$ remain relatively constant in the parameter range considered (Table 1). Increasing q^* with all other parameters fixed shows a general increase in Pe (see also Figure 1), a slight increase in $K_{\mathcal{T}}/K$ and little variation in $K_{\mathcal{T}}^{z}/K$, which is a small fraction of the total energy in all models.

In the next two sections we analyse the models in Table 1 in detail. In the subsequent discussion $\phi = 0°$ corresponds to the rightmost edge of the equatorial projections and is the longitude of minimum heat-flux; the maximum heat-flux is imposed at $\phi = 180°$. The western hemisphere, which is subject to a higher than average heat-flux, is defined as the region $90° < \phi \leq 270°$ and the eastern hemisphere, which is subjected to a lower than average heat-flux, is defined as the region $-90° < \phi \leq 90°$.

3.1. Y_1^1 inner boundary condition

Figure 2 shows four models with $Ra = 90$ that differ only by the value of q^*. The snapshots are taken at time $t = 11$ of Figure 1a. With homogeneous boundaries ($q^* = 0$) the familiar pattern of spiralling columnar rolls aligned with the rotation axis, a feature of moderate Pr and low Ra convection, is obtained (Zhang, 1992). The prograde drift speed of the columns varies with radius and hence the convection is characterised by different wavenumbers at different distances from the rotation axis (e.g. Sun et al., 1993; Tilgner and Busse, 1997). The pattern of temperature anomalies in the equatorial plane is well-correlated with radial velocity. The m-spectrum of kinetic energy (Figure 1) is characterised by a peak at $m = 0$, and broad peaks around the most unstable mode and its overtones.

Imposing a Y_1^1 heat-flux variation at the inner boundary significantly alters the large-scale flow pattern as q^* is increased above zero. For $Ra = 90$ we identify three broad flow regimes. For $q^* \leq 0.6$ the homogeneous flow pattern is modulated by the presence of the Y_1^1 boundary anomaly. Figure 2 shows that, for $q^* = 0.6$, the velocity field in the western hemisphere has a higher amplitude and a larger characteristic azimuthal wavenumber than in the eastern hemisphere. The columnar rolls drift in the prograde sense in this model, but accelerate when passing through the eastern (low heat-flux) hemisphere and decelerate when passing through the western hemisphere. Similar behaviour was found by Zhang and Gubbins (1993) in a convection model with lateral variations at the OB. Temperature anomalies near the IB are predominantly negative in the region $0° < \phi \leq 180°$ and positive in the region $180° < \phi \leq 360°$; a similar phase shift of temperature anomalies with respect to the boundary anomalies has been observed in models of convection with lateral OB variations (Olson, 2003).

For $0.6 < q^* \leq 1.4$ the $m = 1$ mode becomes dominant in the m-spectrum of the kinetic energy (Figure 1) and convection columns are absent in parts of the eastern hemisphere. Very weak radial motions are observed between $-90° < \phi \leq 0°$ as shown in Figure 2 for $q^* = 1.4$. This region is characterised by strong prograde and retrograde azimuthal jets that are established near the IB at $\phi \approx 180°$ and spiral outwards, terminating when they reach the OB. Strong vertical and radial gradients in azimuthal velocity are evident in the region spanned by the jets. The pattern of temperature anomalies is dominated by an $m = 1$ component and strong gradients in the region where the jets are formed.

Finally, for $q^* > 1.4$ the flow patterns are almost stationary as suggested by the kinetic energy time-series in Figure 1a. Figure 2 for $q^* = 4.2$ shows that the azimuthal jets become stronger and have greater lateral extent than at lower values of q^*. The amplitude of vertical and radial gradients in azimuthal velocity in the region spanned by the jets also increase with q^*. Strong upwelling and downwelling regions are visible in the plot of u_r near the locations where the azimuthal jets are initiated and terminated due to interaction with the OB, but away from these regions the radial velocity is very weak. Temperature gradients are strong in the region where the azimuthal jets are formed and departures from the basic state are significant across broad regions of the shell.

The large-scale flow patterns described above for $q^* \geq 1.4$ are reminiscent of those found by Grote and Busse (2001) and Busse et al. (2003) in simulations of rotating convection with homogeneous boundaries. In their models, convection columns are sheared by a strong azimuthal zonal ($m = 0$) flow driven by Reynolds stresses; the zonal flow dominates in large regions of the shell where radial motion is severely inhibited. Although a large-scale shear is apparent in our models for $q^* \geq 1.4$ there are three factors suggesting that it is driven by a different mechanism to that described by Grote and Busse (2001). Firstly, our values of Ra are much smaller than those used by Grote and Busse (2001); indeed, with a homogeneous IB condition and $Ra = 90$, Figure 2 shows that convection columns are not confined to a particular longitudinal band. Secondly, the region where convection columns are observed in the Grote and Busse (2001) simulations is not fixed in space, in contrast to our models where this region remains in the western hemisphere. Finally, our models contain only $\sim 1/10$th of the total energy in zonal components (Table 1), suggesting that the shear generated by large-scale nonzonal flows could greatly exceed shear generated by the zonal flow. We now explore these three points in detail by investigating the mechanisms that drive the azimuthal flows observed for $q^* \geq 1.4$ (Figure 2). We first consider the azimuthal zonal flow, which we denote u_ϕ^z, and then focus on the nonzonal azimuthal flow, which is denoted u_ϕ^{nz} hereafter.

There are two main driving mechanisms for u_ϕ^z (e.g. Cardin and Olson, 1994; Aubert et al., 2003). The first is due to Reynolds stresses arising from the convection columns, which drive a zonal flow with cylindrical symmetry that tends to be strongly retrograde near the IB (Busse, 1970; Cardin and Olson, 1994) and slightly retrograde (Cardin and Olson, 1994) or prograde (Glatzmaier and Olson, 1993) near the OB. The second driving force for u_ϕ^z arises because more heat is lost in equatorial regions than polar regions, which sets up axisymmetric latitudinal temperature gradients that drive zonal flows with shear in the vertical z direction. To distinguish between these two mechanisms we follow Glatzmaier and Olson (1993) and define the geostrophic wind as the portion of the zonal flow that is uniform in the axial direction and the remainder, which contains vertical shear, as the ageostrophic wind. We compute u_ϕ^z by retaining only the $m = 0$ component of the velocity field, and the geostrophic wind, $[u]_\phi^z$ by averaging this flow over z. The averaging operation denoted by square brackets is defined by

$$[] = \frac{1}{2L}\int_L^{-L} \mathrm{d}z, \qquad L = \sqrt{r_\mathrm{o}^2 - s^2}, \tag{10}$$

where $s = r\sin(\theta)$ is cylindrical radius. Figure 3 shows u_ϕ^z and $[u]_\phi^z$ for $q^* = 1.4$ and 4.2. The zonal flow is westward (retrograde) near the tangent cylinder (the imaginary cylinder parallel to the rotation axis that touches the inner core equator) for all values of q^* including $q^* = 0$. Near the OB, u_ϕ^z is slightly prograde at mid-latitudes for low values of q^*; for $q^* \geq 2.8$ the prograde u_ϕ^z at mid-latitudes is approximately half the value of the retrograde flow near the IB. These features are also reflected in the profiles of $[u]_\phi^z$ in Figure 3. Increasing q^* produces a mild increase in u_ϕ^z, presumably due to nonlinear interaction with the large-scale boundary forcing, and also causes an increase in $[u]_\phi^z$; the ratio $[u]_\phi^z/u_\phi^z$ does not show a strong dependence on q^* for the particular Ra we have considered. We conclude that, for the models considered, the geostrophic and ageostrophic contributions to the zonal flow are comparable.

Our models contain a large-scale nonzonal azimuthal flow, u_ϕ^{nz}, that dramatically increases in amplitude as q^* increases (compare the meridional sections in Figures 2 and 3). The variation of u_ϕ with z seen in both Figures suggests a significant thermal wind exists in our models, as has been found in other simulations with inhomogeneous boundary conditions (e.g. Zhang, 1992; Sreenivasan, 2009). Taking the curl of equation (3) with the viscous force and acceleration term omitted gives

$$\frac{\partial \mathbf{u}}{\partial z} + Ra\nabla \times (T\mathbf{r}) - \frac{E}{Pr}\nabla \times [(\mathbf{u}\cdot\nabla)\mathbf{u}] = 0; \tag{11}$$

omitting the contribution from the divergence of the Reynolds stress (the last term) gives the thermal wind balance. Figure 4 shows the terms in (11) and their sum for $q^* = 4.2$. For this model the first two terms in (11) are over an order of magnitude larger than the last term. The remainder after summing terms on the left-hand side of (11) is close to zero outside the tangent cylinder as shown in the rightmost column of Figure 4. These results imply that a thermal wind balance holds for the model with $q^* = 4.2$. Further calculations (not shown) indicate that this balance holds well for all models conducted at $Ra = 90$. Sumita and Olson (2002) noted that regions where $\partial u_\phi/\partial z > 0$ and where $|u_\phi|$ decreases with z imply $u_\phi < 0$ if the thermal wind balance applies. Similarly, $\partial u_\phi/\partial z > 0$ and $|u_\phi|$ increasing with z implies $u_\phi > 0$; $\partial u_\phi/\partial z < 0$ and $|u_\phi|$ decreasing with z implies $u_\phi > 0$; $\partial u_\phi/\partial z < 0$ and $|u_\phi|$ increasing with z implies $u_\phi < 0$. The meridional sections shown in Figure 5 for $q^* = 4.2$ indicate that the above relations are reasonably well-satisfied and further calculations for models that contain large-scale azimuthal jets (see Figure 2) give similar results. These results suggest that, in the models described above, the dominant driving force for the nonzonal azimuthal flow, u_ϕ^{nz}, is a thermal wind. Furthermore, Figure 4 indicates that a thermal wind is the dominant driving force for the ageostrophic contribution to the azimuthal zonal flow, u_ϕ^z.

Figures 3 and 5 show that changes in sign of u_ϕ^z and u_ϕ^{nz} occur at almost the same (cylindrical) radii in regions where radial flow is weak and azimuthal flow dominates, suggesting that shear due to the zonal flow is reinforced by shear due to the nonzonal azimuthal flow driven by the inhomogeneous boundary. This explains why convection columns are not confined to a particular longitudinal band in models with no boundary forcing: shear in the zonal flow alone is not strong enough to break down the convection columns. The region where the columnar rolls can persist is determined by the amplitude of the shear produced by u_ϕ^z and u_ϕ^{nz}. For $q^* \geq 2.8$, u_r and u_ϕ^{nz} are both strongest above the maximum IB heat-flux at $\phi = 180°$, but the shear due to the strong u_ϕ^{nz} is sufficient to break down convection columns directly east of the maximum heat-flux until u_ϕ^{nz} weakens sufficiently for columns to reemerge around $\phi = 0°$. At lower values of q^* the u_ϕ^{nz} driven by the thermal wind is not strong enough to shear convection columns in the western hemisphere where the high heat-flux drives strong radial motions; however, in the eastern hemisphere, the combined action of zonal and nonzonal azimuthal flows dominates over the relatively weak radial motions. This explains why the region where convection columns persist is always located in the hemisphere where the IB heat-flux is higher than the average. Finally, our analysis suggests that the large-scale azimuthal flows in the models described above are driven predominantly by a thermal wind; Reynold's stresses play a secondary role.

For $Ra = 150$ and $Ra = 225$ we did not obtain quasi-stationary solutions for any value of q^* considered. Higher values of Ra lead to more energy in small-scales compared to those with $Ra = 90$, but the large-scale features are very similar to those described above for $Ra = 90$. Figure 6 shows time-averaged flow patterns with $q^* = 1.4$ and $Ra = 90, 150, 225$. Instantaneous and time-averaged flows for $Ra = 90$ show the same basic features, as could be anticipated by comparing the time-averaged and instantaneous velocity spectra in Figure 1. Interestingly, the time-averaged flow for $q^* = 1.4$ indicates that upwellings and downwellings in the western hemisphere, with a characteristic lengthscale much smaller than that of the imposed boundary anomaly, occur in preferred locations. The superposition of scales in flows forced by inhomogeneous outer boundary conditions was noted by Davies et al. (2009). Equatorial sections for $Ra = 150$ and 225 reveal large-scale nonzonal azimuthal flows similar to those studied in detail for $Ra = 90$ and $q^* = 4.2$; indeed, applying the same analysis to these cases suggests that the mechanisms inferred to drive the zonal azimuthal flow u_ϕ^z, and the nonzonal azimuthal flow u_ϕ^{nz}, are the same as those discussed for models with $Ra = 90$. Increasing Ra for fixed q^* does not change the amplitude of u_ϕ^{nz} significantly, but strengthens u_ϕ^z (Table 1) due to increased Reynolds stresses and axisymmetric latitudinal temperature gradients. The combined shear due to u_ϕ^z and u_ϕ^{nz} (which are well-correlated as above) produces similar large-scale effects at $Ra = 150, 225$ as for $Ra = 90$. These results suggest that the behaviour described for solutions with $Ra = 90$ is broadly characteristic of the behaviour across the range of Ra considered.

3.2. Y_1^1 outer boundary condition

In this section we briefly discuss the effect of imposing a Y_1^1 boundary anomaly at the OB with a homogeneous IB. The model parameters are the same as used in §3.1, but we consider only $Ra = 90$. Simulations were conducted with $q^* = 11.2$ and $q^* = 34.2$ (see Table 1), corresponding to OB anomalies that are equal in magnitude to the IB anomalies imposed in the models with $q^* = 1.4$ and 4.2 respectively. No quasi-steady solutions were obtained for models with Y_1^1 OB anomalies at $Ra = 90$, unlike models with Y_1^1 IB anomalies where such solutions were obtained for $Ra = 90$ and $q^* \geq 2.8$. Simulations at higher values of Ra were not conducted, but quasi-steady solutions are not anticipated based on the results of §3.1.

Figure 7 shows a snapshot of the flow pattern for $Ra = 90$ and $q^* = 34.2$. Temporal variations are most apparent outside the tangent cylinder near the IB, where a sequence of columnar rolls reminiscent of the pattern of homogeneous ($q^* = 0$) convection (see Figure 2) drift predominantly in the prograde sense. A cluster of rolls are located beneath the OB under the region of high heat-flux and remain in this location for the length of our simulation (6 time units). A previous study (Davies et al., 2009) with an imposed Y_2^2 OB condition found two such clusters. These results suggest that the number of clusters is determined by the azimuthal wavenumber of the imposed boundary anomaly. Large-scale nonzonal azimuthal flows are generated near the OB but do not penetrate all the way to the IB.

Figure 8 shows the ϕ-component of the thermal wind balance (equation (11)) for $Ra = 90$ and $q^* = 34.2$. Both terms are large and tend to balance near the OB; however, the amplitude of the thermal wind decreases significantly with depth. Conducting the analysis of §3.1 suggests that the large-scale nonzonal azimuthal flows near the OB are driven by the thermal wind resulting from the OB heat-flux anomalies; these flows are much stronger than those obtained with a Y_1^1 IB condition (see Table 1), which we attribute to the larger surface area of the OB giving rise to a stronger thermal wind. Azimuthal flows are much weaker and contain more small-scale structure at depth where the thermal wind is weak. This, together with the fact that the homogeneous system is driven from below, suggests that the effects of OB anomalies do not penetrate far enough into the shell to stop fluid near the IB from drifting, as it would do in the absence of boundary anomalies. For this particular model it appears that the Y_1^1 OB condition has less overall influence on the spatial and temporal characteristics of the flow than a Y_1^1 IB condition. We attribute this to the fact that, in our simulations, the IB condition is imposed in the same location as the buoyancy source for free convection.

4. Discussion and conclusions

We have performed numerical simulations to investigate the effects of a translating inner core on outer core convection. The novel feature of our model is that convection in the outer core is driven non-uniformly from below. Many previous studies have investigated the effects of laterally-varying outer boundary conditions on rotating convection (e.g. Zhang, 1992; Zhang and Gubbins, 1993; Davies et al., 2009) and magnetic field generation (e.g. Olson and Christensen, 2002; Willis et al., 2007; Sreenivasan, 2009) in spherical shells. By contrast, laterally-varying inner boundary conditions have received very little attention, save for an investigation into possible long-term asymmetry in the geomagnetic field by Olson and Deguen (2012). Studies with laterally-varying outer boundary conditions generally use a pattern of boundary anomalies inferred from seismic tomography, a complex combination of spherical harmonics, or the largest harmonic in this pattern, which is Y_2^2. Conversely, the large-scale pattern imposed by inner core translation is a spherical harmonic Y_1^1. Motivated by these issues, we used an idealised nonmagnetic model of thermally-driven convection in a rotating spherical shell designed to highlight the effects of the imposed Y_1^1 inner boundary heat-flux. Nonmagnetic models reduce computational costs, allowing a suite of simulations to be conducted, and afford theoretical simplifications compared to geodynamo simulations. Our results for the simpler hydrodynamic problem will hopefully guide future research into geodynamo models with laterally-varying inner boundary conditions.

The suite of simulations conducted for this work use an Ekman number that is low enough for the dynamics to be rotation-dominated and focus on low Rayleigh numbers, where the influence of the boundary condition is expected to be prominent. Higher Rayleigh numbers could lead to a weakening of boundary effects at the values of q^* (which measures the amplitude of boundary anomalies) used in this work, but higher values of q^* may lead to significant boundary effects even when the Rayleigh number is highly supercritical. Such a regime cannot be ruled out given the significant uncertainties in the value of q^* appropriate for the Earth.

In our models, increasing q^* with all other parameters fixed leads to significant changes in the large-scale flow pattern compared to the solution with a homogeneous inner boundary ($q^* = 0$). The most striking feature is the development of spiralling azimuthal jets that span large portions of the shell. Radial motion tends to be weak where the azimuthal jets are strong. Vigorous convection becomes increasingly confined to localised regions as q^* increases; these regions do not drift and are always located in the hemisphere where the boundary heat-flux is higher than the average.

We explored the processes responsible for generating the localised regions of convection that emerge at large q^*, focusing on shear generated by the large-scale zonal and nonzonal azimuthal flows. Zonal flows generally account for only a small fraction of the total kinetic energy in our models, partly due to our use of no-slip boundary conditions (Christensen,

2002) and partly due to choice of relatively low Ra. The energy in the zonal flow remains a small fraction of the kinetic energy for all values of q^* considered. Large-scale nonzonal azimuthal jets significantly increase in amplitude with q^* and tend to dominate the zonal flows when the boundary forcing is strong. Our analysis suggests that the large-scale nonzonal azimuthal jets are driven by a thermal wind resulting from the boundary anomalies and that the shear generated by these jets leads to the destruction of columnar convection rolls (that would otherwise exist in the absence of boundary anomalies) in regions where the shearing flow is much greater than the amplitude of the radial flow. Thermal winds were found to be more important for driving large-scale flows than Reynold's stresses at high values of q^*.

Applying a Y_1^1 heat-flux pattern at the outer boundary, with a spherically symmetric inner boundary, appears to exert a weaker influence on fluid far from the inhomogeneous boundary compared to a model with the same parameter values and a Y_1^1 inner boundary condition. We suggest that this occurs in the model because outer boundary effects are weakest where the buoyancy force driving homogeneous convection is strongest. Models with inhomogeneous inner and outer boundaries designed to simulate outer core-mantle and outer core-inner core interactions are needed to further explore this potentially significant result.

The effects of the inner boundary condition are visible in instantaneous and time-averaged surface flows even for low values of q^*. Figure 9 shows that the surface expression of the lateral inner boundary anomalies is an amplitude difference between the flow in the eastern and western hemispheres. The amplitude difference increases with q^*. At the highest values of q^* there is a clear signature of the large-scale azimuthal flows that are generated near the inner boundary and spiral outward. Close correspondence between magnetic and non-magnetic flows found in models with laterally-varying outer boundary conditions (e.g. Willis et al., 2007) raise the possibility that flows of this type may arise in geodynamo models. This may be the case if the Lorentz force does not significantly alter the largest scales of the flow.

Our principle conclusion is that the presence of thermal inner boundary anomalies can significantly affect the dynamics of convection in a rotating spherical shell. This result appears consistent with the models of Olson and Deguen (2012), which include the effect of a magnetic field but operate at lower rotation rates than those considered here. Future work is needed to assess the role of laterally-varying thermal inner boundary conditions at rapid rotation rates with the inclusion of the magnetic field.

Acknowledgements

C.D. is supported by a Natural Environment Research Council personal fellowship, NE/H01571X/1. L.S. and J.M. are funded by the Natural Environment Research Council through grant NE/G002223/1. The authors thank Dr. P. Livermore for stimulating discussions.

References

Alboussière, T., Deguen, R., 2012. Asymmetric dynamics of the inner core and impact on the outer core. J. Geodyn. In Press.

Alboussière, T., Deguen, R., Melzani, M., 2010. Melting-induced stratification above the Earth's inner core due to convective translation. Nature 466, 744–747.

Alfè, D., Price, G. D., Gillan, M. J., 1999. Oxygen in the Earth's core: a first-principles study. Phys. Earth Planet. Int. 110, 191–210.

Anufriev, A., Jones, C., Soward, A., 2005. The Boussinesq and anelastic liquid approximations for convection in Earth's core. Phys. Earth Planet. Int. 152, 163–190.

Aubert, J., Gillet, N., Cardin, P., 2003. Quasigeostrophic models of convection in rotating spherical shells. Geochem. Geophys. Geosys. 4.

Braginsky, S., 1963. Structure of the F layer and reasons for convection in the Earth's core. Sov. Phys. Dokl. 149, 8–10.

Braginsky, S., Roberts, P., 1995. Equations governing convection in Earth's core and the geodynamo. Geophys. Astrophys. Fluid Dyn. 79, 1–97.

Buffett, B., 2009. Onset and orientation of convection in the inner core. Geophys. J. Int. 179, 711–719.

Buffett, B., Huppert, H., Lister, J., Woods, A., 1996. On the thermal evolution of the Earth's core. J. Geophys. Res. 101, 7989–8006.

Busse, F., 1970. Differential rotation in stellar convection zones. Astrophys. J. 159, 629–639.

Busse, F., Grote, E., Simitev, R., 2003. Convection in rotating spherical shells and its dynamo action. In: Earth's core and lower mantle. Contributions from the SEDI 2000, The 7th Symposium, pp. 130–152.

Cardin, P., Olson, P., 1994. Chaotic thermal convection in a rapidly rotating spherical shell: consequences for flow in the outer core. Phys. Earth Planet. Int. 82, 235–259.

Christensen, U., 2002. Zonal flow driven by strongly supercritical convection in rotating spherical shells. J. Fluid Mech. 470, 115–133.

Davies, C., Gubbins, D., 2011. A buoyancy profile for the Earth's core. Geophys. J. Int. 187, 549–563.

Davies, C., Gubbins, D., Jimack, P., 2009. Convection in a rapidly rotating spherical shell with an imposed laterally varying thermal boundary condition. J. Fluid Mech. 641, 335–358.

Davies, C., Gubbins, D., Jimack, P., 2011. Scalability of pseudospectral methods for geodynamo simulations. Concurrency Computat.: Pract. Exper. 23, 38–56.

de Koker, N., Steinle-Neumann, G., Vojtech, V., 2012. Electrical resistivity and thermal conductivity of liquid Fe alloys at high P and T and heat flux in Earth's core. Proc. Natl. Acad. Sci. 109, 4070–4073.

Deguen, R., Cardin, P., 2009. Tectonic history of the Earth's inner core preserved in its seismic structure. Nat. Geosci. 2, 419–422.

Deguen, R., Cardin, P., 2011. Thermochemical convection in Earth's inner core. Geophys. J. Int. 187, 1101–1118.

Gibbons, S., Gubbins, D., Zhang, K., 2007. Convection in a rotating spherical shell with inhomogeneous heat flux at the outer boundary. Geophys. Astrophys. Fluid Dyn. 101, 347–370.

Glatzmaier, G., Olson, P., 1993. Highly supercritical thermal convection in a rotating spherical shell: centrifugal vs. radial gravity. Geophys. Astrophys. Fluid Dyn. 70, 113–136.

Grote, E., Busse, F., 2001. Dynamics of convection and dynamos in rotating spherical fluid shells. Fluid Dyn. Res. 28, 349–368.

Gubbins, D., 2001. The Rayleigh number for convection in the Earth's core. Phys. Earth Planet. Int. 128, 3–12.

Gubbins, D., 2007. Dimensional analysis and timescales for the geodynamo. In: Gubbins, D., Herrero-Bervera, E. (Eds.), Encyclopedia of Geomagnetism and Paleomagnetism. Springer, pp. 287–300.

Gubbins, D., Alfe, D., Masters, G., Price, G., Gillan, M., 2003. Can the Earth's dynamo run on heat alone? Geophys. J. Int. 155, 609–622.

Gubbins, D., Alfe, D., Masters, G., Price, G., Gillan, M., 2004. Gross thermodynamics of two-component core convection. Geophys. J. Int. 157, 1407–1414.

Helffrich, G., 2012. How light element addition can lower core liquid wave speeds. Geophys. J. Int., 1065–1070.
Jeanloz, R., Wenk, H., 1988. Convection and anisotropy of the inner core. Geophys. Res. Lett. 15, 72–75.
Kageyama, A., Miyagoshi, T., Sato, T., 2008. Formation of current coils in geodynamo simulations. Nature 454, 1106–1109.
Kennett, B., Engdahl, E., Buland, R., 1995. Constraints on seismic velocities in the Earth from traveltimes. Geophys. J. Int. 122, 108–124.
Labrosse, S., Poirier, J.-P., Le Moeul, J.-L., 2001. The age of the inner core. Earth Planet. Sci. Lett. 190, 111–123.
Lay, T., Hernlund, J., Buffett, B., 2009. Core-mantle boundary heat flow. Nat. Geosci. 1, 25–32.
Monnereau, M., Calvet, M., Margerin, L., Souriau, A., 2010. Lopsided growth of Earth's inner core. Science 328, 1014–1017.
Morelli, A., Dziewonski, A., Woodhouse, J., 1986. Anisotropy of the inner core inferred from PKIKP travel times. Geophys. Res. Lett. 13 (13), 1545–1548.
Nimmo, F., 2007. Thermal and compositional evolution of the core. In: Schubert, G. (Ed.), Treatise on Geophysics, Vol. 8. Elsevier, Amsterdam, pp. 217–241.
Nimmo, F., Price, G., Brodholt, J., Gubbins, D., 2004. The influence of potassium on core and geodynamo evolution. Geophys. J. Int. 156, 363–376.
Niu, F., Wen, L., 2001. Hemispherical variations in seismic velocity at the top of the Earth's inner core. Nature 410, 1081–1084.
Olson, P., 2003. Thermal interaction of the core and mantle. In: Earth's core and lower mantle. Contributions from the SEDI 2000, The 7th Symposium, pp. 1–38.
Olson, P., Christensen, U., 2002. The time-averaged magnetic field in numerical dynamos with non-uniform boundary heat flow. Geophys. J. Int. 151, 809–823.
Olson, P., Deguen, R., 2012. Eccentricity of the geomagnetic dipole caused by lopsided inner core growth. Nat. Geosci. 5, 565–569.
Pozzo, M., Davies, C., Gubbins, D., Alfè, D., 2012. Thermal and electrical conductivity of iron at Earth's core conditions. Nature 485, 355–358.
Souriau, A., Poupinet, G., 1991. The velocity profile at the base of the liquid core from PKP(BC+Cdiff) data: an argument in favor of radial inhomogeneity. Geophys. Res. Lett. 18, 2023–2026.
Sreenivasan, B., 2009. On dynamo action produced by boundary thermal coupling. Phys. Earth Planet. Int. 177, 130–138.
Stacey, F., 2007. Core properties, physical. In: Gubbins, D., Herrero-Bervera, E. (Eds.), Encyclopedia of Geomagnetism and Paleomagnetism. Springer, pp. 91–94.
Sumita, I., Olson, P., 2002. Rotating thermal convection experiments in a hemispherical shell with heterogeneous boundary heat flux: Implications for the Earth's core. J. Geophys. Res. 107.
Sun, Z.-P., Schubert, G., Glatzmaier, G., 1993. Transitions to chaotic thermal convection in a rapidly rotating spherical fluid shell. Geophys. Astrophys. Fluid Dyn. 69, 95–131.
Tanaka, S., Hamaguchi, H., 1997. Degree one heterogeneity and hemispherical variation of anisotropy in the inner core from PKP(BC)-PKP(DF) times. J. Geophys. Res. 102, 2925–2938.
Tilgner, A., Busse, F., 1997. Finite-amplitude convection in rotating spherical fluid shells. J. Fluid Mech. 332, 359–376.
Verhoogen, J., 1961. Heat balance of the Earth's core. Geophys. J. R. Astr. Soc. 4, 276–281.
Waszek, L., Irving, J., Deuss, A., 2011. Reconciling the hemispherical structure of Earth's inner core with its super-rotation. Nat. Geosci. 4, 264–267.
Willis, A., Sreenivasan, B., Gubbins, D., 2007. Thermal core-mantle interaction: exploring regimes for 'locked' dynamo action. Phys. Earth Planet. Int. 165, 83–92.
Woodhouse, J., Giardini, D., Li, X.-D., 1986. Evidence for inner core anisotropy from free oscillations. Geophys. Res. Lett. 13, 1549–1552.
Zhang, K., 1992. Convection in a rapidly rotating spherical shell at infinite Prandtl number: transition to vacillating flows. Phys. Earth Planet. Int. 72, 236–248.

Zhang, K., Gubbins, D., 1993. Convection in a rotating spherical fluid shell with an inhomogeneous temperature boundary condition at infinite Prandtl number. J. Fluid Mech. 250, 209–232.

Zou, Z., Koper, K., Cormier, V., 2008. The structure of the base of the outer core inferred from seismic waves diffracted around the inner core. J. Geophys. Res. 113, B05314.

Ra	q^*	Pe	$K_{\mathcal{T}}$ ($K_{\mathcal{T}}/K$)	$K^z_{\mathcal{T}}$ ($K^z_{\mathcal{T}}/K$)
90	0	38.6	8851 (0.82)	1529 (0.14)
90	0.3	37.2	8162 (0.81)	1258 (0.12)
90	0.6	39.1	9093 (0.82)	1342 (0.12)
90	1.4	45.1	12534 (0.84)	1571 (0.10)
90	2.8	58.2	21689 (0.88)	4014 (0.16)
90	4.2	62.2	24784 (0.88)	4372 (0.16)
90*	11.4	62.8	23972 (0.83)	3814 (0.13)
90*	34.2	79.5	40287 (0.87)	15653 (0.34)
150	0	65.6	26125 (0.83)	3362 (0.11)
150	0.3	65.3	25869 (0.83)	3555 (0.11)
150	0.6	70.1	30392 (0.85)	4855 (0.14)
150	1.4	73.4	33677 (0.86)	5659 (0.14)
150	2.8	77.8	38179 (0.86)	6656 (0.15)
150	4.2	81.8	42048 (0.86)	7881 (0.16)
225	0.3	90.5	48935 (0.82)	7538 (0.13)
225	0.6	89.0	47127 (0.82)	7125 (0.12)
225	1.4	94.2	53996 (0.83)	7811 (0.12)
225	2.8	102.3	64679 (0.84)	11481 (0.15)

Table 1: Convection simulations used in this work. All simulations use $Pr = 1$ and $E = 10^{-5}$. Ra is the Rayleigh number based on the average boundary heat-flux. All models employ a Y_1^1 inner boundary condition and a spherically symmetric outer boundary condition except those denoted with an asterisk, which employ a Y_1^1 outer boundary condition and a spherically symmetric inner boundary condition. Velocity is measured in units of the Péclet number, $Pe = Ud/\kappa = \sqrt{2K/V_s}$, where $V_s = 14.59$ is the nondimensional volume of the spherical shell. K is the total kinetic energy; $K_{\mathcal{T}}$ the toroidal kinetic energy; and $K^z_{\mathcal{T}}$ the zonal toroidal kinetic energy. Each run spans six thermal diffusion time units following an initial transient phase.

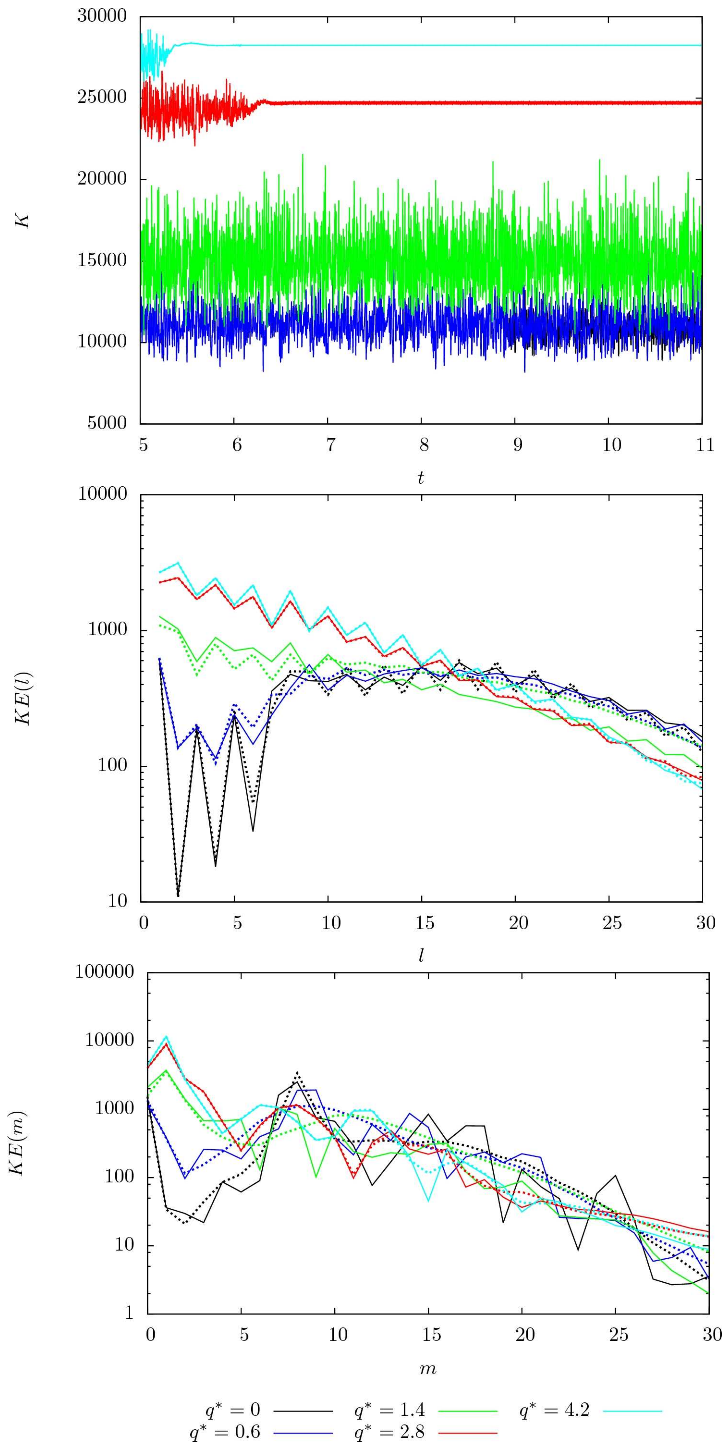

Figure 1: a) kinetic energy plotted against time for different values of q^* (top). Time is measured in units of d^2/κ. b) and c) kinetic energy as a function of harmonic degree l and order m plotted up to degree and order $l = m = 30$ at time $t = 11$ in a) (solid lines) and averaged over the period of time shown in a) (dashed lines). Other parameter values are $E = 10^{-5}$, $Pr = 1$, $Ra = 90$. Note that spherical harmonics up to degree and order 80 were retained in the solutions and spectra are ploted up to $l = m = 30$ for clarity.

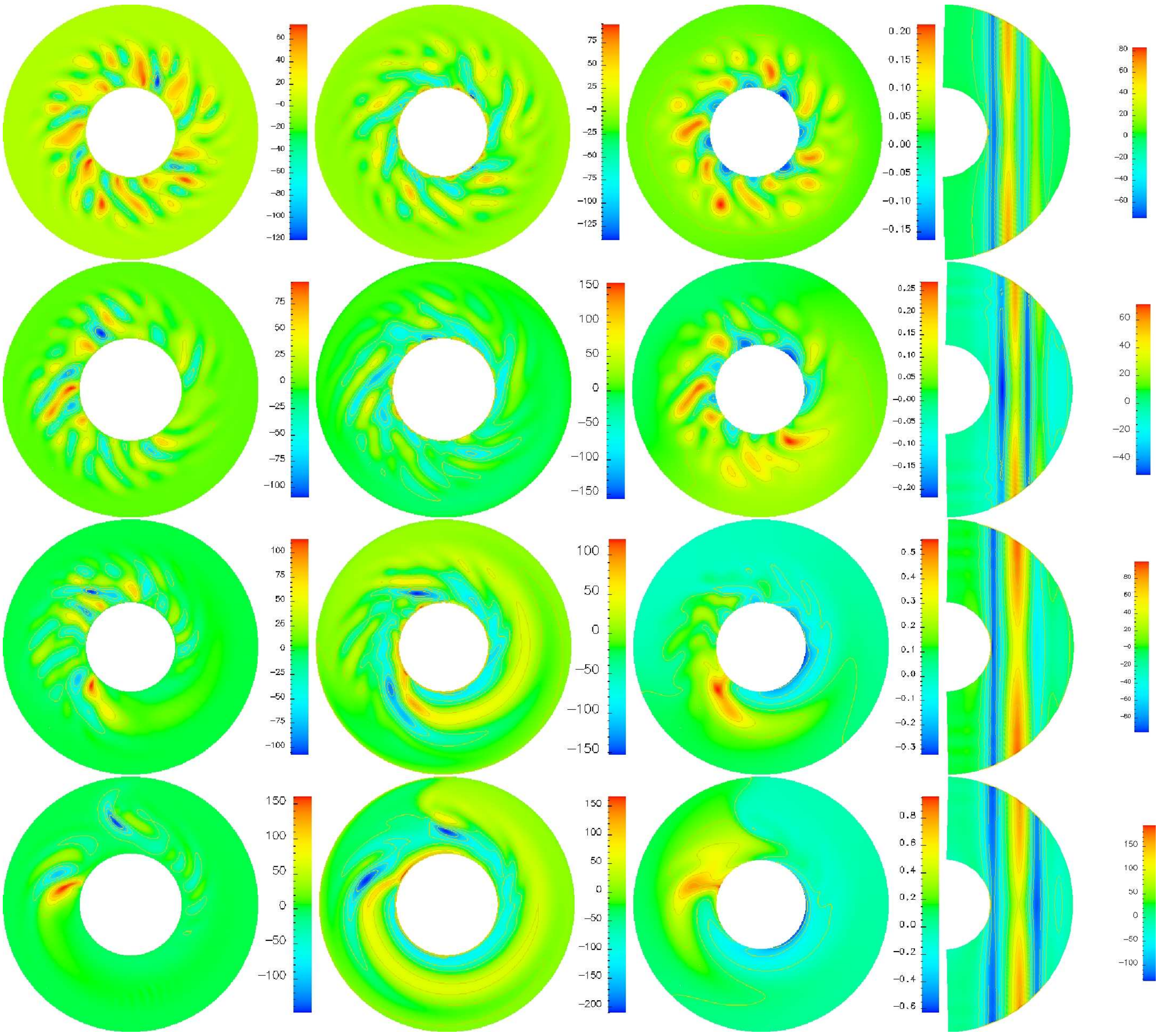

Figure 2: Snapshots of simulations at $t = 11$ in Figure 1a. From top to bottom: models with $q^* = 0$, 0.6, 1.4 and 4.2. Other parameter values are $E = 10^{-5}$, $Pr = 1$, $Ra = 90$. From left to right: u_r in the equatorial plane; u_ϕ in the equatorial plane; temperature perturbation with the spherically symmetric (Y_0^0) component of the spherical harmonic expansion removed; u_ϕ in the meridional plane at $\phi = 270°$. $\phi = 0°$ corresponds to the rightmost edge of the equatorial sections and is the longitude of minimum heat-flux; maximum heat-flux is imposed at $\phi = 180°$.

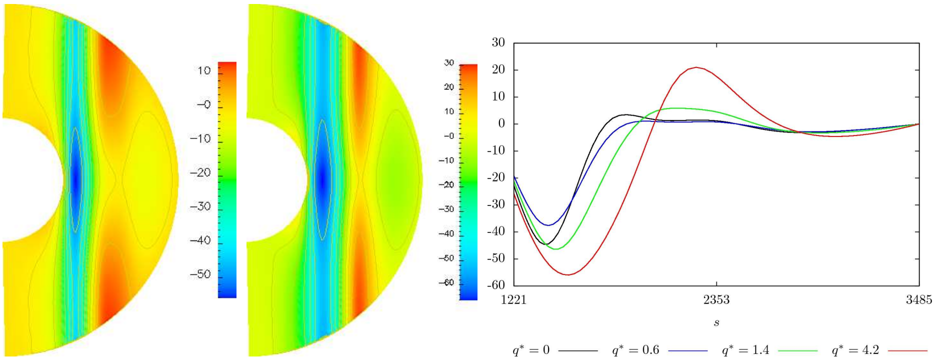

Figure 3: Snapshots of the azimuthal component of the zonal flow, u_ϕ^z, for $q^* = 1.4$ (left) and $q^* = 4.2$ (middle). Snapshots of the vertically (z) averaged azimuthal component of the zonal flow, $[u]_\phi^z$, as a function of radius for various values of q^* (right). Snapshots are taken at $t = 11$ in Figure 1a. Other parameter values are $E = 10^{-5}$, $Pr = 1$, $Ra = 90$.

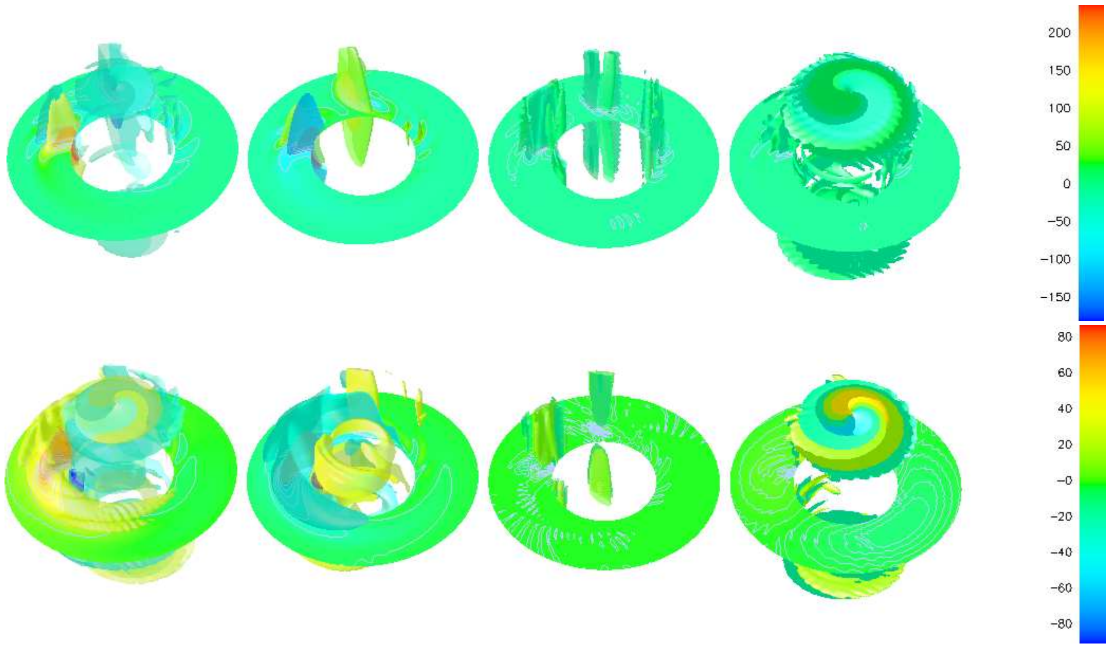

Figure 4: Snapshots, taken at $t = 11$ in Figure 1a, of the θ (top) and ϕ (bottom) components of equation (11) for a model with $E = 10^{-5}$, $Pr = 1$, $Ra = 90$, $q^* = 4.2$ and a Y_1^1 inner boundary condition. The first two columns show the thermal wind balance. The plots show $\partial u_\theta/\partial z$ (column 1, top), $-(Ra/r\sin\theta)\partial T/\partial\phi$ (column 2, top), $\partial u_\phi/\partial z$ (column 1, bottom) , and $(Ra/r)\partial T/\partial\theta$ (column 2, bottom). Column 3 shows the θ (top) and ϕ (bottom) components of the term $(E/Pr)\nabla\times[(\mathbf{u}\cdot\nabla)\mathbf{u}]$ in equation (11). Column 4 shows the remainder after adding the fields in columns 1–3. All images are volume rendered with the equatorial plane highlighted for clarity. Boundary layers have been removed from the plots as they are sources of vorticity, which tend to obscure features in the bulk of the shell.

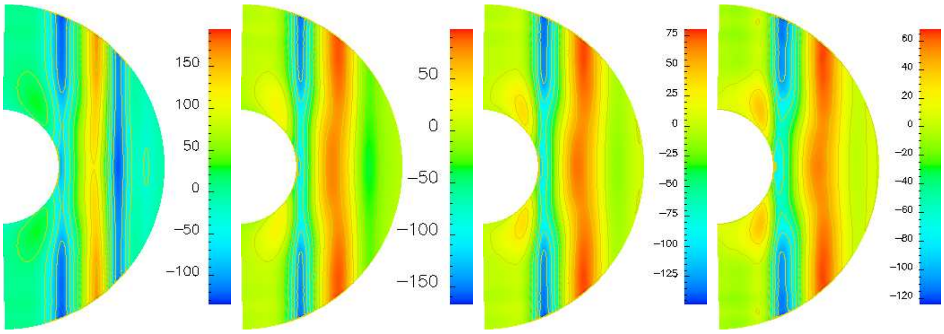

Figure 5: Snapshots of the azimuthal component of the nonzonal ($m \neq 0$) flow, u_ϕ^{nz}, at $\phi = 180°$ (left), 225°, 270° and 315° (right) for $q^* = 4.2$. Snapshots are taken at $t = 11$ in Figure 1a. Other parameter values are $E = 10^{-5}$, $Pr = 1$, $Ra = 90$.

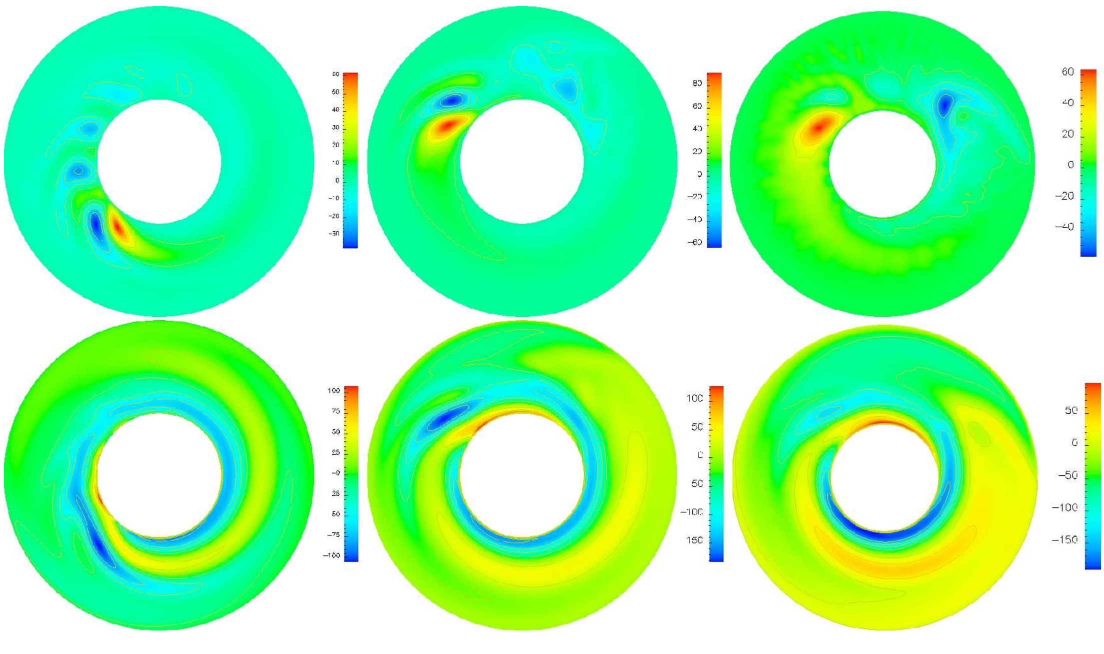

Figure 6: Time-averaged flows for $E = 10^{-5}$, $Pr = 1$ and $q^* = 1.4$. u_r (top) and u_ϕ (bottom) in the equatorial plane for $Ra = 90$ (left), 150 (middle), and 225 (right). Time-averages span 6 time units, which are measured in units of d^2/κ. $\phi = 0°$ corresponds to the rightmost edge of the plots and is the longitude of minimum heat-flux; maximum heat-flux is imposed at $\phi = 180°$.

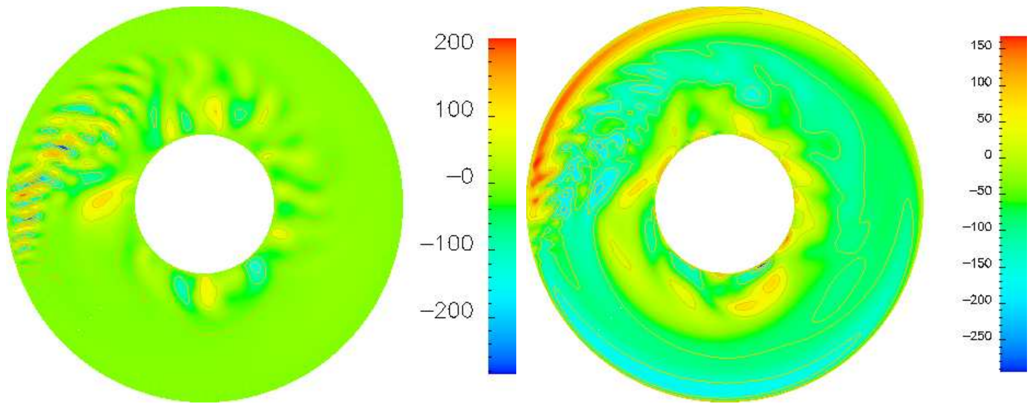

Figure 7: Snapshots of u_r (left) and u_ϕ (right) in the equatorial plane for $Ra = 90$ and $q^* = 34.2$ with a Y_1^1 outer boundary condition. $\phi = 0°$ corresponds to the rightmost edge of the plots and is the longitude of minimum heat-flux; maximum heat-flux is imposed at $\phi = 180°$. Other parameter values are $E = 10^{-5}$, $Pr = 1$, $Ra = 90$.

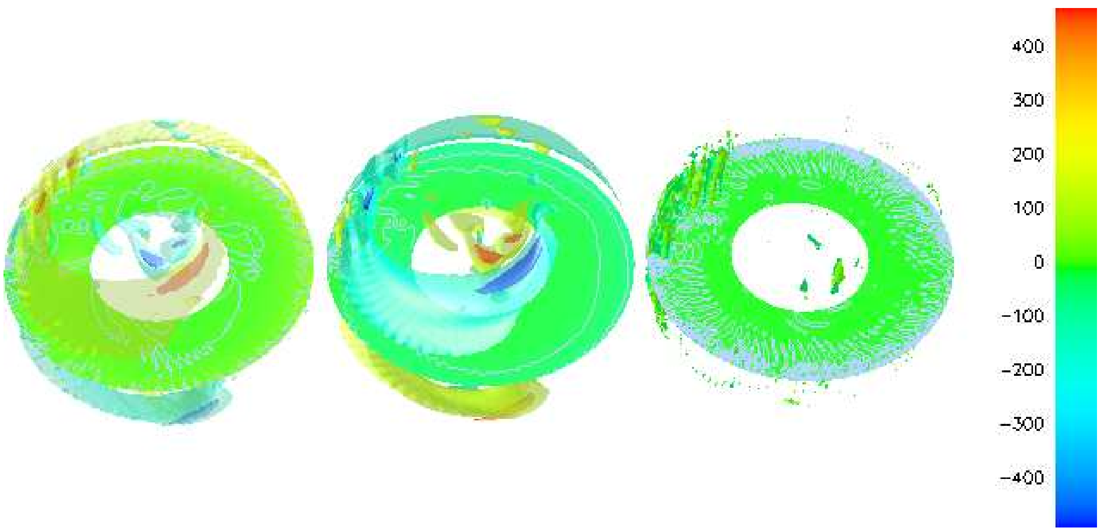

Figure 8: Snapshots of the ϕ component of the thermal wind balance (first two terms in equation (11)) for a model with $E = 10^{-5}$, $Pr = 1$, $Ra = 90$ and $q^* = 34.2$ with a Y_1^1 outer boundary condition. The plots show $\partial u_\phi/\partial z$ (left), $(Ra/r)\partial T/\partial\theta$ (middle), and the remainder after adding the fields in columns 1 and 2 (right). All images are volume rendered with the equatorial plane highlighted for clarity. Boundary layers have been removed from the plots as they are sources of vorticity, which tend to obscure features in the bulk of the shell.

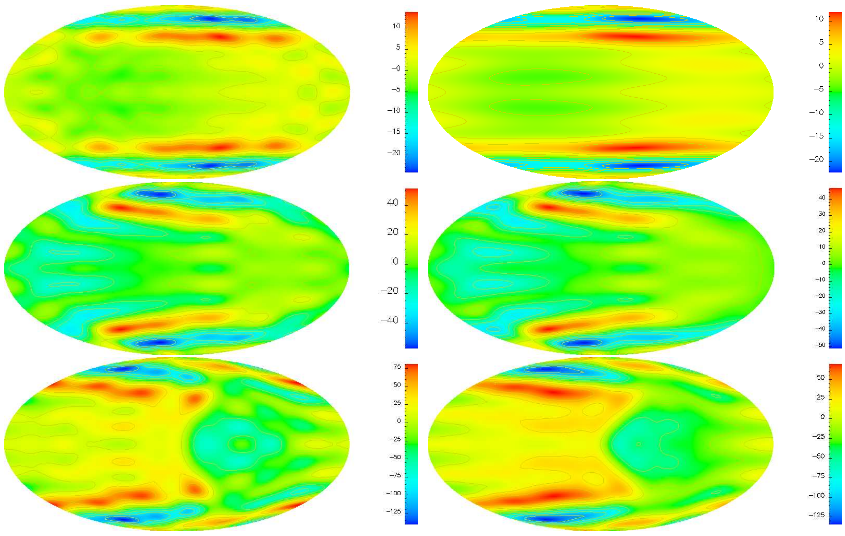

Figure 9: Snapshots (left) and time-averages (right) of u_ϕ in Mollweide projection for $Ra = 90$ and $q^* = 0.3$ (top), $Ra = 90$ and $q^* = 1.4$ (middle) and $Ra = 225$ and $q^* = 1.4$ (bottom). Snapshots are taken at $t = 11$ of Figure 1a. Time-averages span 6 time units, which are measured in units of d^2/κ. Projections are taken at $r = 0.95r_\mathrm{o}$, i.e. just beneath the outer boundary. Note the amplitude difference between the western hemisphere (left half of each projection) and the eastern hemisphere (right half).